Article

An Image-Processing Tool for Size and Shape Analysis of Manufactured Irregular Polyethylene Microparticles

Melanie Fritz [1,*], Lukas F. Deutsch [1], Karunia Putra Wijaya [2], Thomas Götz [2] and Christian B. Fischer [1,3,*]

[1] Department of Physics, Faculty of Mathematics and Natural Sciences, University of Koblenz, Universitätsstr. 1, 56070 Koblenz, Germany

[2] Department of Mathematics, Faculty of Mathematics and Natural Sciences, University of Koblenz, Universitätsstr. 1, 56070 Koblenz, Germany; goetz@uni-koblenz.de (T.G.)

[3] Material Science, Energy and Nano-Engineering Department, Mohammed VI Polytechnic University, Lot 660, Hay Moulay Rachid, Ben Guerir 43150, Morocco

[*] Correspondence: fritz.melanie@web.de (M.F.); chrbfischer@uni-koblenz.de (C.B.F.); Tel.: +49-261-287-2345 (C.B.F.)

Abstract: Microplastics (MPs) pose a significant risk to humans and animals due to their ability to absorb, adsorb, and desorb organic pollutants. MPs catchment from either sediments or water bodies is crucial for risk assessment, but fast and effective particle quantification of irregularly shaped particles is only marginally addressed. Many studies used microscopy methods to count MP particles, which are tedious for large sample sizes. Alternatively, this work presents an algorithm developed in the free software GNU Octave to analyze microscope images of MP particles with variable sizes and shapes. The algorithm can detect and distinguish different particles, compensate for uneven illumination and low image contrast, find high-contrast areas, unify edge regions, and fill the remaining pixels of stacked particles. The fully automatic algorithm calculates shape parameters such as convexity, solidity, reciprocal aspect ratio, rectangularity, and the Feret major axis ratio and generates the particle size distribution. The study tested low-density polyethylene particles with sizes of 50–100 μm and 200–300 μm. A scanning electron microscope image series analyzed with Octave was compared to a manual evaluation using ImageJ. Although the fully automatic algorithm did not identify all particles, the comprehensive tests demonstrate a qualitatively accurate particle size and shape monitoring applicable to any MPs, which processes larger data sets in a short time and is compatible with MATLAB-based codes.

Keywords: microplastic; quantification; particle size distribution; shape classification; scanning electron microscopy; GNU Octave

1. Introduction

A piece of plastic can be categorized into one of several classes depending on its size: macroplastic (<25 mm), mesoplastic (5–25 mm), large microplastic (1–5 mm), small microplastic (20 μm–1 mm), and nanoplastic (<20 μm). This classification has been adopted by the United Nations Environment Programme, the European Marine Strategy Framework Directive, and the National Oceanic and Atmospheric Administration [1], although many other proposals exist [2]. Microplastic (MP) pollution is a global and cross-media issue that has been attracting significant attention from scientific communities, especially in marine and freshwater ecosystems. Many studies raised concerns that MP particles (MPPs) negatively impact animals and humans [2–4]. The hazard potential is highly related to the particle properties; particles of a certain size, shape, or age may more likely be mistaken as food for several species [5–7]. As particles degrade naturally, they become smaller and can easily enter and circulate throughout the body. For instance, evidence suggests that tiny particles can pass through the blood-brain barrier [8,9], while others have been found in the human placenta [10].

To perform a reliable risk assessment of MPPs from both health and environmental perspectives, it is essential to conduct a spatial distribution analysis. To the latter, an easy-to-use and accurate analysis of particle size and shape shall cater to the most crucial step, namely particle quantification. Many methods exist to perform particle size distributions (PSDs) and shape classifications. Examples of spectroscopic techniques include Raman micro-spectroscopy [11,12], focal plane array detector-based micro-Fourier-transform infrared imaging [13–15], field-flow fractionation and pyrolysis gas chromatography–mass spectroscopy [16], proton nuclear magnetic resonance spectroscopy [17,18], and combinations of visual and spectroscopic techniques [19]. To date, there has been no standardized method for analyzing data from MP samples to determine size and shape [20]. Unifying particle size and shape analysis is a major challenge because MPPs are very diverse in their physical and chemical properties. Therefore, not all analytical methods are suitable for every type or size of plastic. Although attempts have been made to establish standardized sampling procedures [21] and identification/quantification methods [22], different practices are often applied. A large amount of uncertainty exists in the literature regarding the most accurate, efficient, and reliable technique for obtaining size measurements of MPPs [23]. Spherical particles can easily be described by their diameter. However, it is still challenging to determine particle sizes when they appear in irregular forms (fibers, fragments, flasks) or in nano-sizes. Polyethylene (PE) particles, one of the most commonly identified irregular MPs, have sizes ranging from 500 μm to 5 mm (pore size of sieves/nets) and can be found ranging from 1 μm to 500 μm (ca. size of filter pores) [24]. Conkle et al. recommended that future studies should concentrate on methods with a diameter of <300 μm to avoid underestimating MP contamination in aquatic environments [25].

Visual sorting is one of the most used methods for identifying MPPs based on criteria such as type, shape, degradation stage, and color [14,22,26]. Microscopic sizing is another method that involves observing and measuring individual particles by comparing their two-dimensional projected area with a known reference. Random alignment on the slide is required to obtain representative results, which may sometimes be difficult. Scanning electron microscopy (SEM) produces images that contain a two-dimensional projection of the recorded particles. If the particles have different lengths in all three dimensions, it can be assumed that the direction of the shortest extension is parallel to the microscope. The recorded projection perpendicular to the electron beams shows the longest extensions of the particles [24]. In addition to directional bias, all microscopy methods are carried out on extremely small samples, requiring high throughput for statistically meaningful results.

Furthermore, inadequate sample preparation often leads to overloading and overlapping particles that may be misinterpreted as a single particle during image processing. However, direct imaging is considered one of the best options among other techniques because semi-automatic and automatic development systems are highly sped, less tedious, and less error-prone [27]. In contrast, non-imaging measuring methods, such as dynamic light scattering or small-angle X-ray scattering, do not provide precise particle forms [28]. An important requirement for image quality is avoiding factors that can negatively impact it, such as poor lighting conditions, noise, low contrast, and poorly defined boundaries, among other parameters [29]. Common image analysis studies typically focus on microstructural analysis of materials, such as metals. This analysis is useful for determining parameters such as grain boundaries, grain size, and grain size distribution, which are important for determining mechanical properties like strain, ductility, and stress resistance [29]. However, few studies have investigated whether microscopic methods could serve as a rapid screening method for MPPs [30,31].

The classification of microplastic shapes is a neglected area of research that yields few published findings. Altuhafi et al. investigated particle size and shape in their geotechnical research by quantifying digital images of sand particles. They considered shape parameters such as convexity, sphericity, and aspect ratio [32]. Chen et al. quantified MP fibers in PLA-lined plastic cups by counting, sizing, and analyzing morphology using Nile Red and ImageJ version 1.53 k [33]. Sample preparation and observation techniques for the

characterization of MPs or NPs in aquatic environments using SEM/EDS is an appropriate procedure [34]. Cabernard et al.'s study emphasized the importance of combining optical microscopy with spectroscopic techniques, such as infrared and Raman scattering, for precise chemical identification of MPs [35].

Shape analysis has been a field of research found in pharmaceutical technology, geology, food processing, railway construction, and cosmetic products, amongst others [36–39]. However, several shape parameters based on area or perimeter have been ideated to quantify deviation from geometric standard objects like circles, ellipses, rectangles, and convex polygons. The use of isotropic particle models with circular 2D projections is not sufficient as the only descriptor of MPs, so other shape parameters must be analyzed to describe the shape of MPPs [38]. For example, Kooi et al. simplified the characteristics of MPs, such as size, shape, and density, as three-dimensional probability distributions to enhance understanding of their environmental risk [40]. Characterizing MPs is crucial for reliable data interpretation, effective risk assessment, and understanding their pathways of distribution, sources, and sinks [41,42]. The counting of NPs in marine bioindicators was proved in principle by Valsesia et al. [43]. Their presented algorithm can also be established for NPs when microscopic images of the NPs are available.

Examining the correlation of particles with basic geometric objects is an unusual approach to shape description that is seldom found in the literature. When applied, authors typically use shape parameters as decision thresholds [44]. Igathinathane et al. conducted successful tests and identified multiple shape parameters that were good predictors for shape. They developed a routine that uses these shape parameters to find thresholds that provide the best agreement with previous methods used in food grain analysis [36]. Irregular particles are often modeled using fitting ellipses to characterize particle shape [45]. Non-automated digital image analysis is widely considered to be a time-consuming process due to the need for manual image-to-image evaluation to accommodate varying image contrast, brightness, scale, format, or particle loading [29]. Additionally, precise preparation is required to prevent particle agglomeration. The identification of individual particles requires separability to enable meaningful digital image processing. The improved watershed feature can now effectively segment slight-to-medium particle contacts [46].

Other potential methods for segmenting highly overlapping particles include using a U-Net-based deep learning segmentation network [47] or the method developed by Moaveni et al. [37]. However, there are still challenges to be addressed in standardizing a fast and cost-effective method for analyzing MPs [48,49]. Whether this information is provided by screening methods based on visual identification or a combination of analytical methods does not matter, but they should be reasonably accurate. Schwaferts et al. investigated the possibility that very small MPs on the Raman filters might not be detected [50]. They presented a measurement algorithm that automatically stops if an appropriate number of particles are identified. Various techniques are available for particle recognition and morphological characterization, including Raman microspectroscopy. Efforts are being made to compare analytical methods, such as Raman spectroscopy and FTIR, for the quantification of MPs [51].

Furthermore, Raman spectroscopy was combined with SEM/EDS investigation for further analysis [52]. This study characterized manufactured plastic MPs and compared them to environmental MPs, as conducted by Kefer et al. [53]. Only a few studies have developed a new program for the automated detection, quantification, and morphological characterization of MPs using SEM images [54].

This work addresses the gap in automation by using the free software GNU Octave version 6.1.0. The program successfully identifies rough polyethylene particles from SEM images, with robustness against slight variances in image quality, such as noisy and unevenly illuminated backgrounds. Shape parameters, including convexity, solidity, reciprocal aspect ratio, rectangularity, and Feret major axis ratio, were used, cf. [37,38]. The best practice for identifying the size and shape of irregularly manufactured low-density polyethylene (LDPE) was employed. Characterizing MPs is crucial for interpreting data

and understanding their behavior in the environment. The type and size of microplastics are key factors in their adsorption and uptake by aquatic organisms [41]. The LDPE used in this study was previously characterized in a caddisfly larvae uptake study using μFTIR microscopy, including size and shape [55]. Although the type of polymer used is not crucial, its rough surface presented challenges in characterization due to the non-closed particle surfaces. The algorithm presented here can be applied to any other microplastic, down to the nanoscale, using high-resolution microscopic images.

2. Materials and Methods

2.1. Materials and Sample Preparation

The study examined two batches of low-density polyethylene (LDPE) resin pellets, Riblene MV10R, manufactured by Versalis, (Milan, Italy), and distributed by TER Plastics Polymer Group (Herten, Germany). The grinding particle size of the pellets was investigated, with one batch having a size (i) smaller than 300 μm and the other (ii) smaller than 800 μm. The LDPE used was an industrial sample provided free of charge. Both LDPE particle sample batches were sieved by a vibratory sieve shaker (Fritsch Analysette, Fritsch GmbH, Idar-Oberstein, Germany) with mesh sizes per sieve ranging from 500 μm down to smaller than 50 μm (amplitude 3 mm, interval duration of 5 s for 3 min of total sieving time). After the sieving process, each fraction, as listed in Table 1, was carefully collected, transferred to an individual sample container, stoppered, and stored in a dry location. For the development and testing of the algorithm, all sieve fractions ranging from 300 μm down to 50 μm were utilized (highlighted with bold font in Table 1).

Table 1. List of the LDPE particle fractions from batches (i) <300 μm and (ii) <800 μm. The stated mesh size range in μm refers to the particle sizes retained by the respective sieve. Fractions highlighted in bold font were used for further analysis.

(i) LDPE Fractions < 300 μm, Mesh Size [μm]	(ii) LDPE Fractions < 800 μm, Mesh Size [μm]
	>500
	400–500
>300	**300–400**
200–300	**200–300**
150–200	**150–200**
125–150	**125–150**
100–125	**100–125**
50–100	**50–100**
25–50	

Prior to SEM imaging, the samples were evenly distributed with a spatula on a smooth surface cleaned with isopropanol (99%, CHEMSOLUTE®, Th. Geyer GmbH & Co. KG, Renningen, Germany). The SEM sample carriers were prepared using a double-sided adhesive carbon pad (Plano G3347, Plano GmbH, Wetzlar, Germany) that was then pressed onto the particles. If too many particles were stacked on top of each other during visual inspection, the procedure was repeated using a freshly glued sample carrier. The prepared sample carriers were stored in SEM storage boxes to prevent air contamination.

2.2. Scanning Electron Microscopy

The LDPE samples underwent imaging using a scanning electron microscope (Phillips SEM 515, FEI Company, Amsterdam, The Netherlands) after being coated with a thin gold layer for 1 min (30 mA, distance 50 mm, coating thickness ca. 14 nm; BAL-TEC SCD 040, BAL-TEC GmbH, Schalksmühle, Germany) to avoid charging effects. At least five images per LDPE sample were taken at different locations for each magnification (MAG, 20×, 50×, 110×, 221×, 442×, 885× and 1770×). The samples were recorded by two different operators using the SEM software INCA version 7 at an acquisition speed of 79.3 s. One

operator created JPG images with a resolution of 1024 × 768 px (8-bit, RGB), while the other created TIF images with a resolution of 1406 × 1026 px (CYMK).

2.3. Software and Digital Image Processing (DIP)

The open-source platform GNU Octave version 6.1.0 was used for DIP under Windows 10 Pro (RAM 16.0 GB, Intel® Core™ i7-7500U CPU @ 2.70 GHz 2.90 GHz, 64-Bit). The package *image* and the non-supported *matgeom* were used to perform morphological and geometric operations were used. The scale bar in the original SEM images using the free software GNU Image Manipulation Program GIMP 2.8.22 (Spencer Kimball, Peter Mattis and team) [25]. The algorithm was modified for the DIP as described in the Supplementary Materials, SI1. Specifically, the scripts, Script S1: MP_Analysis_Particle.m and Script S2: MP_Analysis_Particle_RGB.m were developed to accommodate the different formats (see Section 2.2). For versatility tests, the algorithm written in Octave was run with MATLAB (The MathWorks, Inc. R2021b, Natick, MA, USA) operating on a macOS system. A manual evaluation using free software ImageJ version 1.53 k (Wayne Rasband, National Institutes of Health, Bethesda, MD, USA) was carried out to validate the algorithm's results. The user manually set the parameters to accurately detect particle contours, ensuring that particles touching each other were correctly separated and recognized as individual particles, and any incorrectly detected artifacts were manually sorted out. The SEM analysis was conducted on LDPE particles at 20×, 50× and 110× magnification to ensure full visibility of particles based on their size. Figure 1 provides a schematic overview of the individual steps of the DIP, which are explained in detail below and visually supported in Figures 2 and 3.
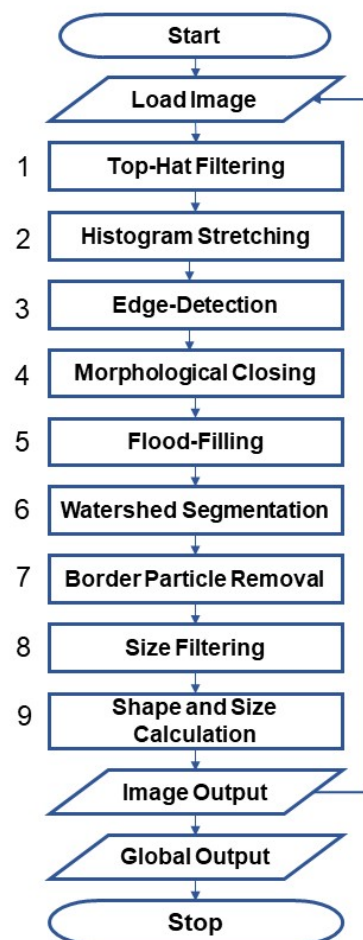
Figure 1. Flowchart of the developed algorithm according to steps 1 to 9 explained in the text.
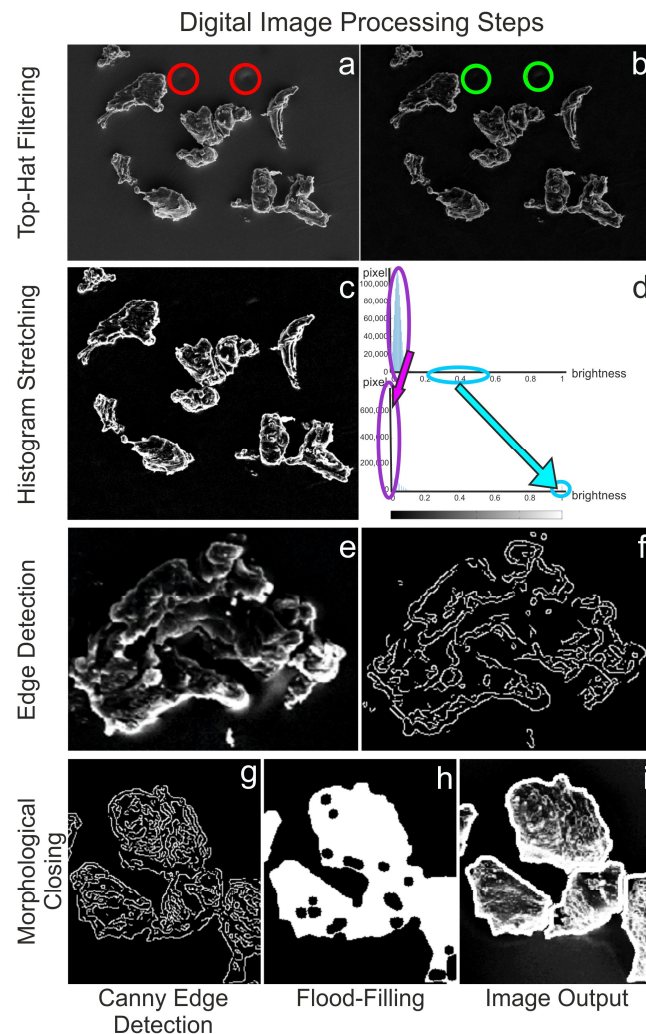
Figure 2. Original image with disturbing background artifacts (red circles) (**a**) and top-hat filtered image with eliminated disturbing factor (green circles) (**b**). Image after histogram stretching (**c**) and corresponding pixel brightness distribution before (**d**, **top**) and after (**d**, **bottom**) stretching, where the purple and light blue circles with the corresponding arrows indicate the shifts. Single LDPE particle before (**e**) and after using *Canny* edge detection (**f**). Image after *Canny* edge detection (**g**), after morphological closing (**h**), and final detected particles after "Flood-Filling" (**i**).

The DIP starts with the *Load Image* command, as shown in Figure 1.

(1) The first step involves using the "Top-Hat Filtering" command *imtophat* to suppress noise in the image background (Figure 2a,b).

(2) The subsequent step is "Histogram Stretching" (*imadjust*) to increase contrast (Figure 2c). To stretch the histogram (Figure 2d), the formula (Equation (1)) requires determining the minimum (f_{min}) and maximum pixel intensity (f_{max}) and multiplying them by the levels of gray (255 levels) where f(x,y) denotes the value of each pixel intensity.

$$g(x,y) = (f(x,y) - f_{min})/(f_{max} - f_{min}) \times 255 \tag{1}$$

(3) Two "Edge-Detection" methods, *Canny* and *Sobel*, were tested and compared to identify the LDPE particles: edge detection and global thresholding (*Otsu*) (see Supplementary Materials, SI2. Global thresholding versus edge detection, Figure S1). *Canny* was chosen for further processing (Figure 2e–g).

(4) The extracted edges were finished using "Morphological Closing" (*imclose*), which grows the edges (*dilation*) and then shrinks them (*erosion*) using *disk* as a structuring element [56,57].

(5) The binary images' lights were filled out using "Flood-Filling" (*imfill*) to eliminate holes (Figure 2h,i).

(6) The "Watershed Segmentation" (*watershed*) was then used to separate LDPE particles that were touching or overlapping (Figure 3a,b).

(7) To determine particle size, only fully displayed particles were considered. This required removing all particle regions touching the image border using "Border Particle Removal" (*imclearborder*) (Figure 3c,d).

(8) In the subsequent step of "Size Filtering", a priori information on the analyzed sieve fraction (Tables 1 and 2) was utilized. To define the minimum/maximum size of eligible particles (*bwareaopen*), the metric size was converted to digital units (see later Section 2.4, Equation (5)) before excluding particles that were too small/large (Figure 3e,f).

(9) The final and most crucial step, "Shape and size calculation", is explained in detail in Section 2.4 *Implemented formula*. The final step of the process is a special feature that superimposes the detected particle outlines onto the input image for visual inspection (*imerode*) (Figure 3g,h). This helps the user better evaluate the accuracy and performance of the algorithm. The script concludes with the *Global Output* command plotting diagrams and data lists. For more information on DIP, please refer to references [56,57]. The complete commented scripts used for the following size and shape analysis can be found in the Supplementary Materials (see Section SI1). The developed scripts, Script S1: MP_Analysis_Particle.m and Script S2: MP_Analysis_Particle_RGB.m are included.
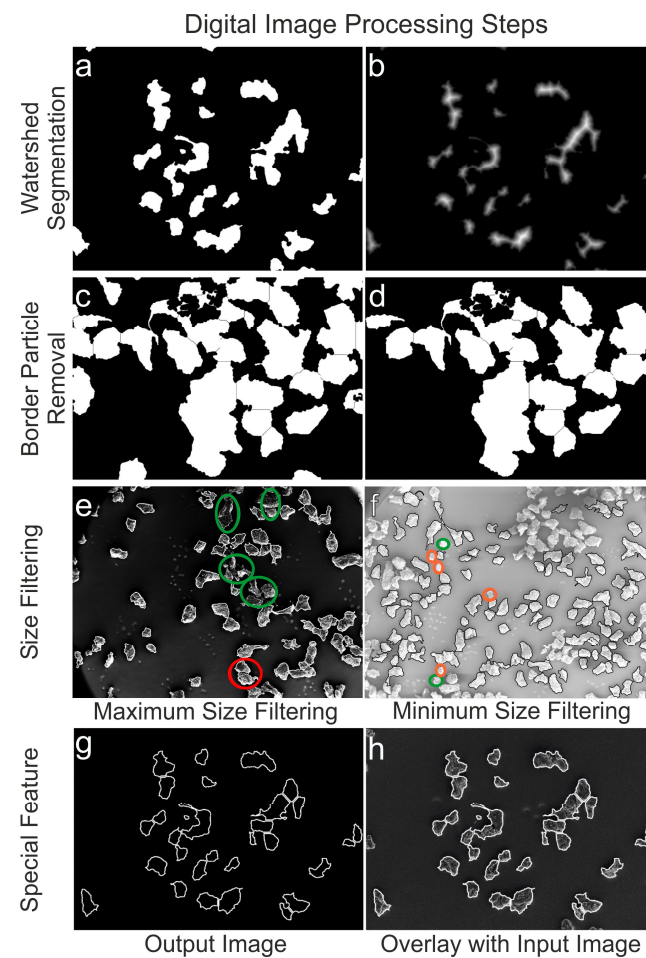
Figure 3. Binary input image before watershed segmentation (**a**) and after (**b**). Watershed image before clearing the border (**c**) and after particle removal (**d**). Maximum size filtering with excluded agglomerates (green circles) and counted ones (red circles) (**e**). Minimum size filtering with excluded particles (green circles) and excluded parts of over-segmented particles (orange circles) (**f**). Particle outlines of the output image (**g**) and its overlay with the input image for visual inspection (**h**).

Table 2. The four "best" settings (A–D) for the tested image series.

Settings	Total Particles	Identified Particles	Total Errors	Identification Ratio [%]	Error Ratio [%]
A		472	81	51.4	17.2
B	95	513	97	55.8	18.9
C		409	76	44.5	18.6
D		498	120	54.2	24.1

2.4. Implemented Formula

2.4.1. Watershed Segmentation

To perform watershed segmentation, the Euclidian distance metric is first applied to the binarized input image. This metric h(x,y) measures the distance of the nearest background pixel (px). Any px considered to belong to the background is automatically assigned a binary value of zero, and the foreground px are weighted accordingly. Mathematically, the distance transformation produces a surface S with a z-component represented by the distance function h(x,y), where x and y refer to the px position (Equation (2)):

$$S: [0,x_{max}] \times [0,y_{max}] \rightarrow \mathbb{R}^3, (x,y,z)^T = (x,y,h(x,y))^T \tag{2}$$

An Octave-specific limitation is that *bwdist* considers the binary value "1" as background and "0" as object area. To amend this, the input image must be inverted before performing the distance transformation. The minima of the calculated surface S are called catchment basins, which are later used as potential watersheds to segment overlapping or touching particles at the points where they are most likely to be contiguous. The function *watershed* only identifies the mountain ridgelines, so the catchment basins need to be transformed into ridge lines first. The quality of the calculated watershed segmentation depends on the tested objects. Optimization was necessary for the tested LDPE particles due to their irregular shape and rough surface texture. To avoid irregular particles tending to generate a multitude of smaller extrema in the distance transform (over-segmentation) (Figure 4a,b), an optimization of the normal watershed segmentation was required. The H-maxima transform (*imhmax*) with the parameter H as a threshold to determine the minimum distance for a px to be considered a maximum was used. This operation sets all px below the threshold to "0" and subtracts the threshold value H from px containing a value above H. The subsequent function (*imregionalmax*) retains the px that contains the local maxima within a region. The retained maxima were used as markers, so the distance map only possesses regional maxima in locations where the markers were placed using morphological reconstruction. Since this function only exists in GNU Octave for minima, the distance map matrix containing the distance values for each px is given the negative sign before being processed (*imimposemin*). This enhancement results in a more correct separation of overlapping or touching LDPE particle regions (Figure 4c,d). Usually, a priori knowledge about the particle shape is used for further improvements. Since the script is intended for universal MP shapes, no geometry restriction was made.
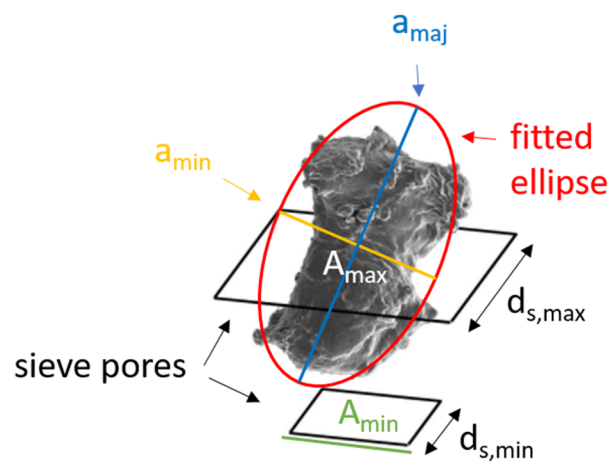
2.4.2. Particles and Sieve Pores

SEM images were used to develop "Size Filtering" with LDPE particles of sieve fractions 50–100 µm and 200–300 µm (batch < 800 µm, Table 1). The principle is demonstrated in Figure 5, assuming that the particles passing through the sieve pores have an elliptical longitudinal section. The model parameters were used to derive the minimum (A_{min}) and maximum particle area (A_{max}). Particle analysis of all available images showed that 95% of the particles resemble ellipses. The fitted ellipses' ratio of minor (a_{min}) to major axis (a_{maj}) is greater than 0.33. Furthermore, it is assumed that the maximum longitudinal section of these "elliptical" particles (A_{max}) has a minor axis a_{min} that fits exactly through the square pores of the sieves (maximum length $d_{s,max}$).
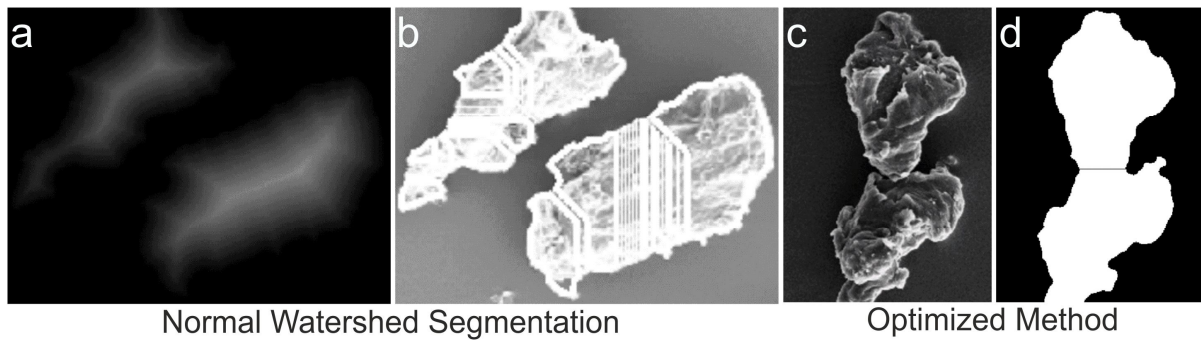
Figure 4. Distance map with multiple local maxima within a region (**a**), resulting in severe over-segmentation using normal watershed segmentation (**b**), SEM image of two overlapping LDPE particles (**c**), which could be successfully segmented with the optimized method (**d**).

Figure 5. Shown are two different-sized sieve pores (black squares) and an LDPE particle that can pass through the first but not the second sieve pore. The area of the smaller sieve pore is expressed by A_{min} (green) and of the bigger sieve pore with A_{max} (white), their distances with $d_{s,min}$ and $d_{s,max}$, respectively. The red circle indicates the fitted ellipse onto the particle with minor axis a_{min} (yellow) and major axis a_{maj} (blue).

Accordingly, the considered particles have a major axis length of $a_{maj} = 3 \times d_{s,max}$ and A_{max} is given by Equation (3):

$$A_{max} = \pi \times (d_{S,max}/2) \times 3 \times (d_{s,max}/2) = (3/4) \times \pi \times d^2_{S,max} \qquad (3)$$

For particles that are too large to fit through the sieve pores (with a minimum length $d_{s,min}$), a rectangular shape corresponding (A_{min}) to an ideal sieve pore is assumed. To account for the dynamic nature of the sieving process and the possibility of particle abrasion, breakage, or elastic deformation, an extra 5% is applied in Equation (4).

$$A_{min} = 1.05 \times d^2_{S,min} \qquad (4)$$

The assumption in this model was based on the fact that the particles had been previously sieved. Figure 3e,f demonstrate the effect of the maximum and minimum size filtering. Size filtering lowers the number of detected particles and the error in incorrectly segmented particles. It is worth questioning whether the advantages outweigh the disadvantages; however, it is important not to overlook the possibility, as information on size and shape is often available for MPs through sampling methods such as filter pores and fishing gears.

2.4.3. Particle Size Determination

For particle size determination, the identified particle regions must be evaluated individually using the *regionprops* command. The particle area specified in px must be converted to μm^2 using the appropriate conversion ratio. To determine this ratio, the length scale was quantified using GIMP. By knowing the ratio of horizontal metric length (n in μm) to px length (d) and assuming that px^2 has a quadratic form (A_{px}, a square of n^2 μm^2 equals d^2 px^2), Equation (5) can be used to derive the area conversion ratio:

$$\alpha = (n/d)^2 \times [\mu m^2/px^2] \tag{5}$$

For a given particle size A_{px} (in px^2), the conversion factor α converts the digital area to the equivalent metric area A_m (in μm^2) as shown in Equation (6):

$$A_m = \alpha \times A_{px} \tag{6}$$

The particle size distribution (PSD) within a single image is then returned by creating and saving an image of the corresponding bar chart at five equidistant intervals. Since graphical objects cannot be saved directly to a file in Octave, a workaround must be taken. The graph must be created in a figure and then automatically saved, resulting in a potential loss of information and slowing down the algorithm. Therefore, this method for analyzing SEM image series is supplemented by the creation of a CSV file. This allows for more flexible access to statistics when examining large data sets.

2.4.4. Particle Shape Analysis

The developed algorithm calculates four different shape parameters and plots and stores the PSDs for single images and image series. The shape parameters used to analyze the LDPE particles were convexity, solidity (SOL), reciprocal aspect ratio (RAR), rectangularity (REC), and Feret major axis ratio (FMR). Two different methods ((I) and (II), see below) were tested to classify the shape of the model particles.

(I) The first method uses the shape parameters RAR, FMR, and REC (Equations (7)–(9)). The RAR is defined as the minor axis length (a_{minor}) divided by the major axis length (a_{major}) of fitted ellipses:

$$RAR = a_{minor}/a_{major} \tag{7}$$

The REC is the area of the enclosed particle $A_{particle}$ divided by the area of the bounding box (L_{BB} length and W_{BB} width), which is a non-inclined rectangle that completely encloses the particle:

$$REC = A_{particle}/(L_{BB} \times W_{BB}) \tag{8}$$

The FMR describes the maximum distance between two parallel lines ($d_{f,max}$ = Feret maximum diameter), each line touching the perimeter in exactly one point divided by a_{major}:

$$FMR = d_{f,max}/a_{major} \tag{9}$$

To calculate $d_{f,max}$, all vertices of the particle convex hull must be taken and the maximum distance of all vertices must be found. After returning the vertices of the convex hull (n possible pairs, command *regionprops*), a calculation with a brute force algorithm is possible (n^2 distance calculations and selection of the maximum value) [42,43].

From the studies of Igathinathane et al. [34], the thresholds for classification into ellipses, rectangles, and triangles were determined using the RAR, REC, and FMR values. Classification into circles and squares was not performed because these are special cases of ellipses and rectangles, respectively. Particles that could not be unambiguously assigned to any geometric shape formed a fourth "inconclusive" category.

(II) Another common method to describe the shape of irregular LDPE particles is to calculate convexity and solidity as shape parameters. The convexity of the shape perimeter

is defined in Equation (10) as the ratio between the perimeter of the convex particle hull (P_{hull}) and its perimeter (P_{perim}):

$$convexity = P_{hull}/P_{perim} \qquad (10)$$

The convexity cannot be calculated error-free in Octave but in MATLAB. For debugging purposes, a perfectly T-shaped object with a known perimeter of 318,000 px was created in GIMP. Octave calculated a perimeter of 305,702 px, and MATLAB returned the correct values using the same script. The bug could not be fixed, so the convexity results obtained with Octave are not shown in this work.

The SOL in Equation (11) describes the ratio of the particle area ($A_{particle}$) to the convex hull area ($A_{convexhull}$) in the interval (0,1], where 1 is convex:

$$SOL = A_{particle}/A_{convexhull} \qquad (11)$$

More details about these shape parameters can be found in the literature [58–60].

3. Results and Discussion

3.1. Pilot Testing

3.1.1. Particle Geometry

For shape classification, particles are usually fitted to a known geometric object and shape parameters are deduced from this. It was therefore examined whether the particles most closely resembled an ellipse, a rectangle, or a triangle or must be classified as "inconclusive" (see Section 2.4.4). The verification shows that only a very small number of particles were classified as "inconclusive", and no particle was identified as triangular (Figure 6). The special feature projects the adjusted ellipses and corrected rectangles onto the centroids of the detected particles, thus allowing a user-based evaluation. Particles with concave shapes were sometimes identified as rectangular, and particles with nearly rectangular outlines with little distortion were sometimes identified as ellipses. Changing the decision thresholds did not improve agreement. The tendency to identify particles as ellipses increases with decreasing particle size and accuracy of particle outline, as illustrated by a comparison of shape analysis of the same group of particles in 20× and 110× MAG (Figure 6c,e). It is evident from these tests that the particle shapes are elliptical rather than rectangular and very rarely triangular or inconclusive.
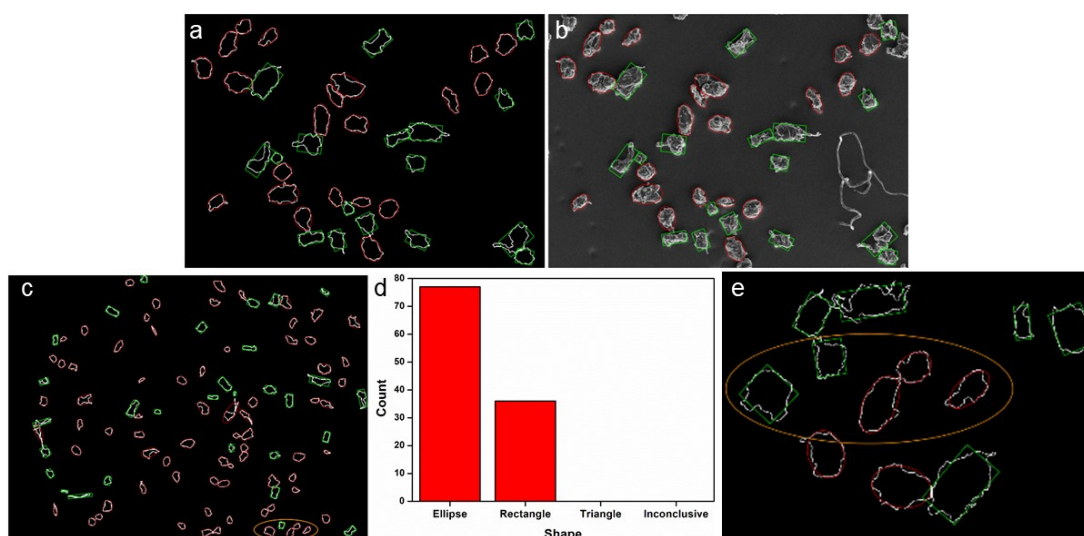
Figure 6. LDPE particles identified as rectangular (green) and elliptical (red) (**a**), overlay of the geometric outlines with the input image (**b**); in 20× MAG, the elliptical shape predominates, followed by the rectangular (**c,d**) and in 110× MAG the geometric classification changes (circled area) (**e**).

3.1.2. Evaluation of "Best" Setting

The functionality of a fully automatic particle analysis relies on careful consideration of settings that affect the outcome of image processing in terms of accuracy and computation time. An optimal choice is challenging, as conflicting effects must be weighed. SEM images vary in terms of illumination, brightness, particle coverage etc. (Figure 7a,b).
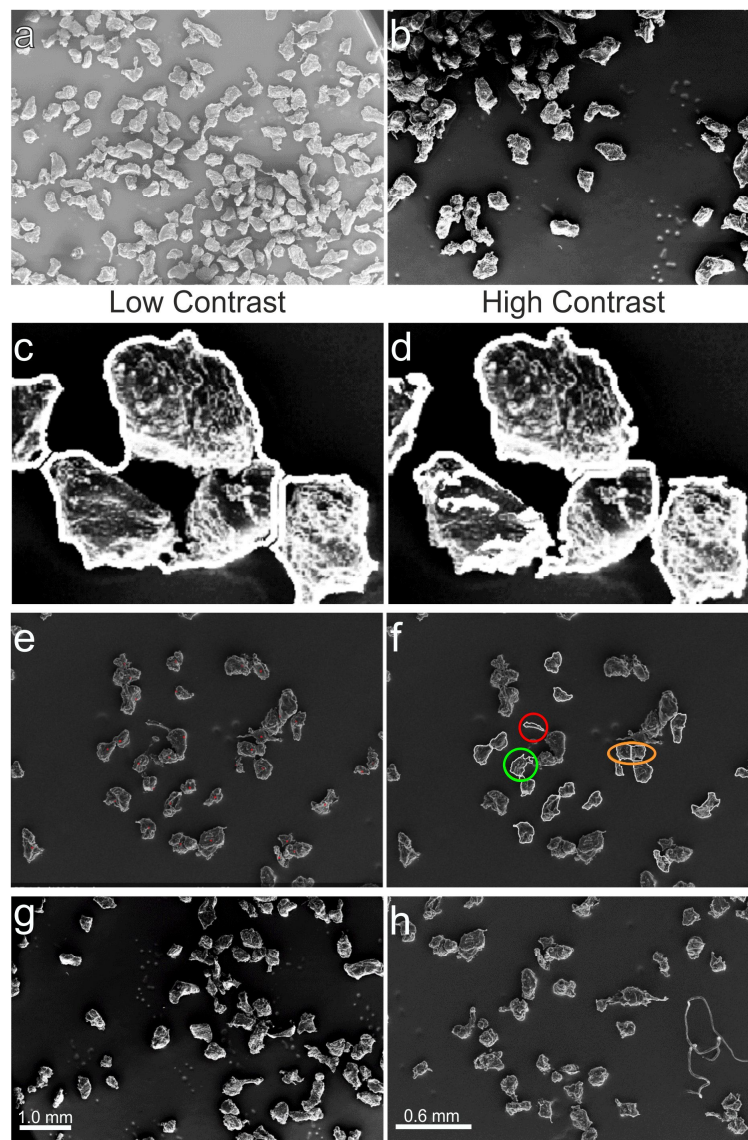
Figure 7. Bright SEM image with high particle coverage (**a**), unevenly illuminated image with lower coverage and higher contrast (**b**), unsuccessfully closed edges of the same particle agglomeration (**c**,**d**), counted LDPE particles (red marked) and highlighted scenarios (green, red, and yellow circled) to explain counting criteria (**e**,**f**), two pilot SEM images at 20× (**g**) and 50× (**h**) MAG.

To address this, the proposed algorithm must be robust against variations in image quality, especially noisy and unevenly lit backgrounds. The key settings identified during implementation are divided into three categories: (1) threshold value of the h-maximum transform, (2) particle model used, and (3) size of the structuring elements. Structuring elements are used to perform top-hat filtering, morphological closing of detected edges, and creation of the particle outline overlay. Figure 7 shows the consequences when morphological closure has failed because the structural element is too large (Figure 7c) or too small (Figure 7d).

The counting criteria method used for the visual inspection is illustrated in Figure 7e,f. The red circled particle was detected as an extension of the large particle (one error). The orange circled particles were classified as one particle in the visual analysis but over-segmented into two smaller particles by the algorithm (two errors). The green circled particle's outline slightly touches the neighboring particle on the right, and the antenna-like extension makes up only a small part of the particle. Here, the algorithm worked (0 errors).

Before testing the algorithm for an image series (a total of 11 images), numerous settings were tested using two pilot images (Figure 7g,h). The remaining 13 respectable settings (see Supplementary Materials, Section SI3. Evaluation of "best" setting, Tables S1 and S2) were narrowed down to four combinations. A more detailed list of the generated data to evaluate the "best" settings can be seen in the Supplementary Materials (see SI3. Evaluation of "best" setting, Tables S3–S6). The summarized results are shown in Table 2, with the four "best" settings (A–D) taken from Tables S2 and S3: rows 1–4. Information about the tested setting values can be viewed in the same supporting (Tables S2 and S3, columns 1–3).

A comparison of the settings (Table 2) showed that (B) and (D) feature a similar identification ratio, with B being superior in terms of the error ratio of 18.9% against 24.1% (D). Therefore, (D) was discarded for the fully automatic algorithm setting.

On the other hand, (C) posed a slightly better error ratio of 18.6% but only identified 44.5% of all visually counted particles compared to the 55.8% that (B) detected. For the visual inspection method, each considered particle was marked with a red dot (Figure 7e) and particle outlines were detected by the algorithm with highlighted scenarios (red, orange, and green circled) (Figure 7f).

Thus, (C) was eliminated as an optimal setting. Setting (A) featured a slightly lower identification and error ratio compared to (B). When looking at the total errors, (B) detected an extra 41 particles but also misidentified 16 more particles than (A). The better accuracy of (A), therefore, led to the choice of using it as the best setting for fully automatic analysis. The difference between the two settings is a higher threshold for local extrema, which results in fewer segmentations being performed. This, in turn, leads to fewer errors overall. Setting (C) has a segmentation threshold of 5 and a low error rate. However, fewer particles were identified because morphological closure is performed more aggressively. This results in a larger number of agglomerations being filtered out by exceeding the maximum particle size.

3.1.3. Influences of Magnification Changes

To determine whether identical particles seen through a microscope at different magnification (MAG) levels match in size, particles found on the SEM images in MAG 20× (reference) and partially recovered in 50× and 110× were evaluated, and the analytical data were compared. The selected particles were mostly isolated to avoid influences of the watershed transformation. MAG 20× was used as a reference, in which all selected 27 particles (No. 1–27) are numbered (Figure 8a–c). Of these particles, 13 (No. 15–27) were detected at MAG 50× (Figure 8d,e), and the remaining 14 particles (No. 1–14) were observed on three SEM images at MAG 110× (Figure 8f–h). $A_\%$ is defined as the deviation of particle size in percentage for MAG 50× or 110× in relation to MAG 20×. Particles from three different images at MAG 20× were analyzed and compared to five images at higher MAGs. Statistics were calculated for the reference MAG-specific subsamples and for individual images (Figure 8a–e).

A summary of the statistical data is presented in the Tables 3 and 4. The size measurements and deviation from the baseline of each particle are shown in Supplementary Materials (SI4. Influences of magnification changes, Table S7). The statistics (Table 3) show that the particle sizes of the subsamples MAG 50× and 110× differ from the reference (MAG 20×) with $-(18.8 \pm 1.9)$%. Considering the subsample MAG 110×, the difference $A_\%$ becomes more significant with $-(22.3 \pm 1.8)$%, while the uncertainty is even smaller. For the subsample MAG 50×, the difference $A_\%$ is $-(15.0 \pm 3.1)$% with a higher degree of uncertainty. Table 4 reveals that the lower negative difference and higher degree of

uncertainty come mainly from image (d: MAG 50×, No. 15–20). The particle measurements in this image agree well with the reference (MAG 20×). However, on average, a single particle and thus its entire subsample deviates from the reference by $-(4.0 \pm 2.0)\%$. Excluding Figure 8g and forming a subset of the particles from Figure 8d–f,h, the deviation is $-(23.0 \pm 1.3)\%$, showing the highest homogeneity. In the calculations performed, it was assumed that the particle area is a two-dimensional area, and the deviation is homogeneous in both dimensions.
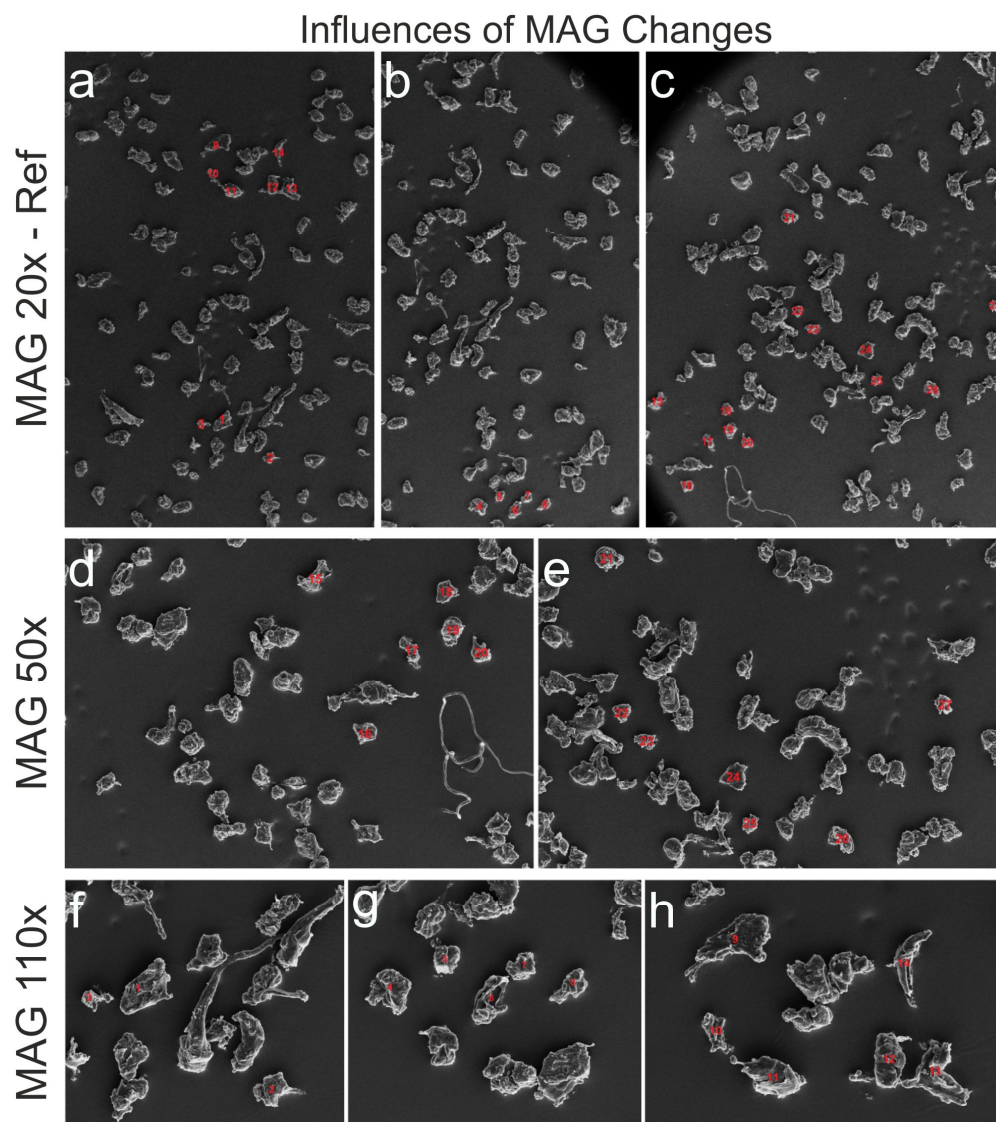
Figure 8. SEM image series showing selected particles (with red numbers) recorded at MAG 20× (reference) (**a–c**) (No. 1–27) and identical particles imaged at MAG 50× (No. 15–27) (**d,e**) and MAG 50× (No. 1–14) (**f–h**) for testing the influences of MAG changes.

Table 3. Statistics for the overall sample at MAG 20× and subsamples at MAG 50× and 110×.

Sample	MAG 20× (Baseline)	MAG 50×	MAG 110×
Mean $A_\%$ [%]	-18.8 ± 1.9	-15.0 ± 3.1	-22.3 ± 1.8
Std. dev. σ [%]	9.8	11.3	6.7

Table 4. Statistics for the images presented in Figure 8d–h.

SEM-Image	(d)	(e)	(f)	(g)	(h)
Mean $A_\%$ [%]	-24.2 ± 2.2	-4.0 ± 2.0	-24.6 ± 1.5	-22.8 ± 4.2	-19.9 ± 3.8
Std. dev. σ [%]	5.3	4.9	3.6	7.3	8.6

Thus, the error introduced for the particle area is quadratic. One source of uncertainty is probably the resolution of the digital images. The images provided have a resolution of 1406 px × 1026 px (~1.4 million px^2). The side of a px at MAG 20× has a length of 5.3 μm, while at MAG 50× it measures 2.1 μm. Considering a square test object with an area A and sides of metric length n, an error of only one px at MAG 20× leads in the worst case to a maximum deviation of (21.2·n + 112) μm^2 (per side (n + 10.6) μm). This increases the deviation linearly with object length n. However, this cannot explain the absolute differences in the 4-digit range, assuming a particle length of 10–20 px that is known from the sieving. The stable deviation of about 20% must be caused by other factors. *Canny* edge detection generally overestimates particle size by a few px in all directions. The error caused by this effect does not increase further with MAG 110× compared to MAG 50×, as might be expected. This suggests that the deviation is caused by other variables. Therefore, for accurate sizing, it is necessary to calibrate each MAG level against a standard instead of using the measuring bar as a reliable conversion factor.

3.2. PSDs and Shape Classification for the 1st Series of Known Sieve Fractions

The determined "best" setting (Table 2 (A)) was used for a fully automatic test run of a small image series (here called the 1st series). The 1st series tested (11 images shown in Supplementary Materials, SI3. Evaluation of "best" setting, Figure S2) contained LDPE particles of the known sieve fractions 50–100 μm and 200–300 μm in MAG 20× and MAG 50×. Both fractions were evaluated individually to compare the PSDs within each sieve fraction. In the 50–100 μm fraction studied, 70% of the 223 LDPE particles detected have an area size in the range of 1.2–2.4 × 10^4 μm^2 (Figure 9a).

Assuming a spherical particle fitting exactly through the sieve pores of this size class has a cross-sectional area of 0.8 × 10^4 μm^2 and thus lies at the 20th percentile of the PSD. As a result, most of the investigated particles (~80%) were expected to have an elongated shape with a_{minor} ~100 μm of the fitted ellipse (Equation (7)). This should result in a highly right-skewed RAR distribution, which was not the case (Figure 9c). For the 200–300 μm sieve fraction, more than 90% of the evaluated 249 particles had a size of less than 1.4 × 10^5 μm (Figure 9b). This is twice the size of the cross-section of a spherical object that narrowly fits through the sieve pores. Most particles were found in the class between 0.5–0.6 × 10^5 μm^2, which is slightly above the lower limit of acceptable particle sizes. Beyond this value, a general decrease in particle frequency is observed, with a sharp drop at 1.4 × 10^5 μm^2. The PSD is skewed towards the lower end. The RAR distribution of the LDPE particles in the 50–100 μm size fraction had a slight left-skewed tendency, while that of the size fraction 200–300 μm showed a mild right-skew (Figure 9c,d).

Assuming a minor axis of 100 μm, 40% of the LDPE particles would be expected to have a RAR of less than 0.5. This is not the case, as only 20% of the MPs are below this value. The result strongly suggests that many of the MPs in the 50–100 μm fraction are larger than 100 μm in the direction of their second-largest dimension. The FMR distributions (Figure 9e,f) have a mean of ~1.05 for both sieve fractions with a mostly Gaussian distribution. In general, a larger mean of the FMR indicates that convex hull of the particles is more elongated compared to the major axis of the fitted ellipse, describing irregular particle shape in the direction of the longest extension. The SOL distributions (Figure 9g,h) show that the LDPE particles from the 200–300 μm batch did not achieve agreement above 96% between particle and convex hull area. They also do not represent particles below a value of 0.6, which is the case for several particles from the batch 50–100 μm. Particles with very low SOL values are often incompletely identified (smaller 0.6). A more detailed comparison

between the PSDs determined by the DIP and those obtained by the sieve method is not made. Since sieve PSDs are reported as a percentage of the total mass in each size range, the results cannot be directly compared to the PSDs discussed above. Furthermore, sieve analysis is not exact either (e.g., clogging, electrostatic charge effects, quality of sieves, etc.).
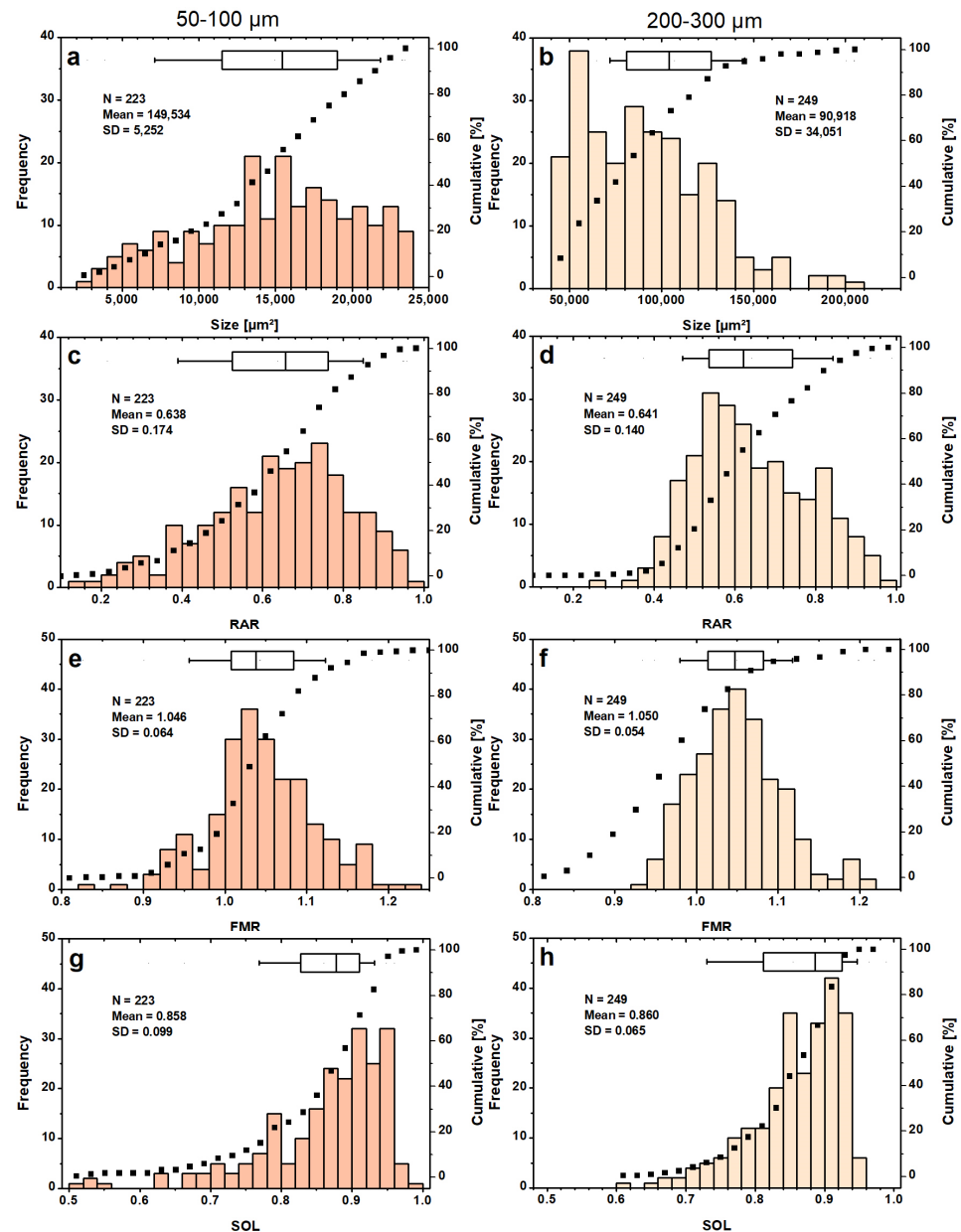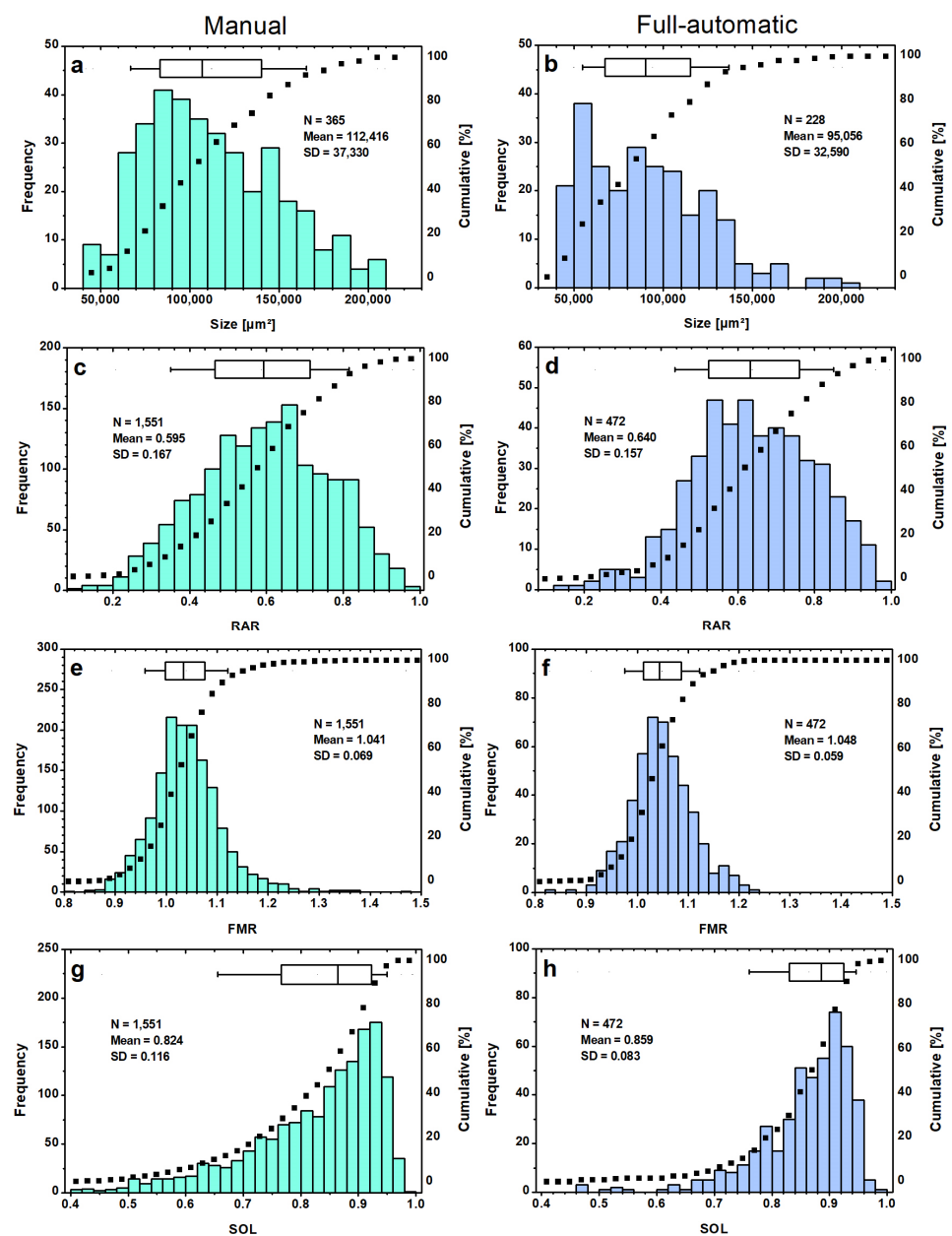

Figure 9. PSDs of the sieved LDPE particles (**a**,**b**) with corresponding shape parameters RAR (**c**,**d**), FMR (**e**,**f**) and SOL (**g**,**h**) for sieve fractions 50–100 μm (**left column**) and 200–300 μm (**right column**) for the 1st series. The dotted curves represent the cumulative value in percent, which refers to the right axis. The boxplots display the 25% and 75% percentiles, with the whiskers at 0% and 90%.

3.3. Evaluation of the Same Sieve Fraction Full-Automatic and Manual

The algorithm was subjected to another endurance test (2nd series) to see its limitations. The PSD (Figure 10a) is based on 10 images (see Supplementary Materials, SI5. Second image series, Figure S3) evaluated manually by ImageJ. The median is at 1.11×10^5 μm², and the extended peak spans from 0.8×10^5 μm²–1.0×10^5 μm². Only 5% of the 365 detected MPs were measured smaller than 0.6×10^5 μm². A rapid increase in particle frequency can be seen at the lower end of the size class spectrum. This is followed by a slow

decline in the class population for the larger particles detected 2.1×10^5 μm². The difference is also notable in the higher median particle size of 1.11×10^5 μm² against 0.95×10^5 μm² in favor of the manually evaluated series. The fully automatic evaluated PSD (Figure 10b) shows again the analyzed LDPE particles of the sieve fraction 200–300 μm from the 1st series (Figure 9b). Since manual counting is very time-consuming (note: each particle outline was traced by hand with a pencil), only this fraction is compared. Comparison of the 90th percentiles results in a value of 1.38×10^5 μm² for the fully automatic analysis and 1.65×10^5 μm² for the manual one. This highlights the higher proportion of larger particles and a slower decline in frequency after surpassing the peak. The major difference is the concentration of particles at the lower scale, which is caused by the *Size Filtering* of the algorithm.

Figure 10. PSDs of LDPE particles for the sieve fraction 200–300 μm evaluated manual (ImageJ, **left column**) and fully automatic (Octave, **right column**) (**a,b**). The shape distributions of the parameters RAR (**c,d**), FMR (**e,f**) and SOL (**g,h**) are based on the 2nd series for manual evaluation (I-series, **left**) and of merged sieve fractions (50–100 and 200–300 μm) of the 1st series (O-series, **right**).

For the manual shape classification (Figure 10c,e,g), the two batches (<300 and <800 μm) of the LDPE particles (see Supplementary Materials, SI5. Second image series, Figures S4 and S5, 2nd series, in total 43 images with detected 1551 particles) were combined, called the I-series, then compared to the fully automatic classification by ImageJ, which evaluated 1st series of the two sieve fractions 50–100 μm and 200–300 μm, called the O-series, for better comparison (see Supplementary Materials, SI3. Evaluation of "best" setting, Figure S2). The classification of particle shapes shows a similar range for the RAR parameters (Figure 10c,d), although the I-series contains more particles with a lower RAR ratio. This means that more elongated particles could be detected manually. The mean value is given as (0.595 ± 0.004) for the I-series (Figure 10c), which is 0.045 lower (0.640 ± 0.007) than for the O-series (Figure 10d). Half of the particles of the O-series are between 0.520–0.760, which describes fitted ellipses with an a_{major} ~33–100% larger. When comparing the FMR distributions (Figure 10e,f), a wide span with a minimum of 0.82 and a maximum of 1.48 was revealed for the I-series, which is more than 0.2 larger than the largest value encountered in the O-series. The mean of the FMR distribution is (1.041 ± 0.002) for the I-series, meaning 0.007 lower than the O-series (1.048 ± 0.003). Another difference is the lower degree of symmetry. The peak of the FMR distribution is wider, and the particle frequency decreases more slowly towards larger values, resulting in a slightly right-skewed trend for the I-series (Figure 10f).

A comparison of the SOL distributions (Figure 10g,h) reveals that a larger number of LDPE particles with low SOL values are present in the I-series. 15% of the identified I-series particles have SOL values below 0.7, while the O-series contains only 5% of the particles in this range. For the O-series, the SOL distribution is more left-skewed, with 70% of the particles having a value between 0.820 and 0.960. The median is 0.859 compared to the median value of 0.824 for the I-series. Particles with low SOL often have an irregular shape or may indicate incorrect particle identification.

Overall, the shape distributions (Figure 10c,e,h) of the particles analyzed in the I-series exhibit similar distributions compared to the O-series (Figure 10d,f,h). The small differences are visible at the distribution tails, indicating a higher number of misidentifications and unfiltered errors. However, the main differences are due to the fact that the setting used for the analysis of both series was based on the 1st series. The goal of achieving the best performance for the 1st series resulted in the size and segmentation thresholds of setting A (cf. Section 3.1.2). The "best" setting should not be determined based on such a small image series.

Further pilot tests are needed to make it more suitable for diverse MP samples. In addition to the differences in sample preparation and SEM imaging by different users, the algorithm had to be adapted to the different image formats, magnitudes, sizes, and color spaces. A disadvantage when using JPG format is always the compression (resolution of JPG: 1024 × 768 px against TIF: 1406 × 1026 px). For better understanding, each pixel corresponds to an area of 28.30 μm^2 (TIF) compared to 40.40 μm^2 (JPG) area per pixel for an image taken in MAG 20×. This also influences the results. In summary, the main errors are due to different imaging quality and considering an insufficient number of settings or test samples.

3.4. Visual Inspection of Fully Automatic Analyzed Image Series

To understand how the poorer quality of an image series (due to format, contrast, LDPE coverage, etc.) influences the fully automatic analysis, the detection rate of 15 images in JPG-format of the LDPE particles <800 μm batch was analyzed by the algorithm. The evaluated images are summarized in the Supporting Information (see Supplementary Materials, SI5. Second image series, Figure S5). All misidentified particles were counted through visual inspection, and the identification and error ratios were evaluated as before (cf. Section 3.1.2). The algorithm was expected to correctly identify a lower percentage of MPs due to the lower image quality. At least three images of each of the sieve fractions listed in Table 5 were analyzed.

Table 5. Results of the visual inspection. The designations A and B are used here to distinguish between different samples of the same sieve fraction.

Sieve Fractions [μm]	Total Particles	Identified Particles	Total Errors	Identification Ratio [%]	Error Ratio [%]
125–150	396	166	43	41.9	25.9
150–200 A	151	87	32	57.6	36.8
150–200 B	219	133	39	60.7	29.3
200–300	270	137	44	50.7	32.1
Sum	1036	523	158	50.5	30.2

As expected, the algorithm identified 0.9% less particles in this series compared to the 1st one. The observed error ratio has increased from 17.2% (for best setting A, Table 2) to 30.2% in sum (Table 5). Several factors influence this decrease in accuracy. Compared to the 1st series, more particles are incompletely detected. Some consequences of low contrast can be seen in Figure 11. The selected contrast was not sufficient for successful edge detection and must be increased accordingly. This leads to the conclusion that the algorithm cannot be used universally without manual adaptation to image contrast, size, resolution and format. To run through a larger number of images, a consistent image format and similar quality must be given, and a smaller data set should be visually inspected to check the identification and error ratio. This adjustment of the settings can be easily remedied by a few test runs and checking whether the particle contours of the input and output images match.
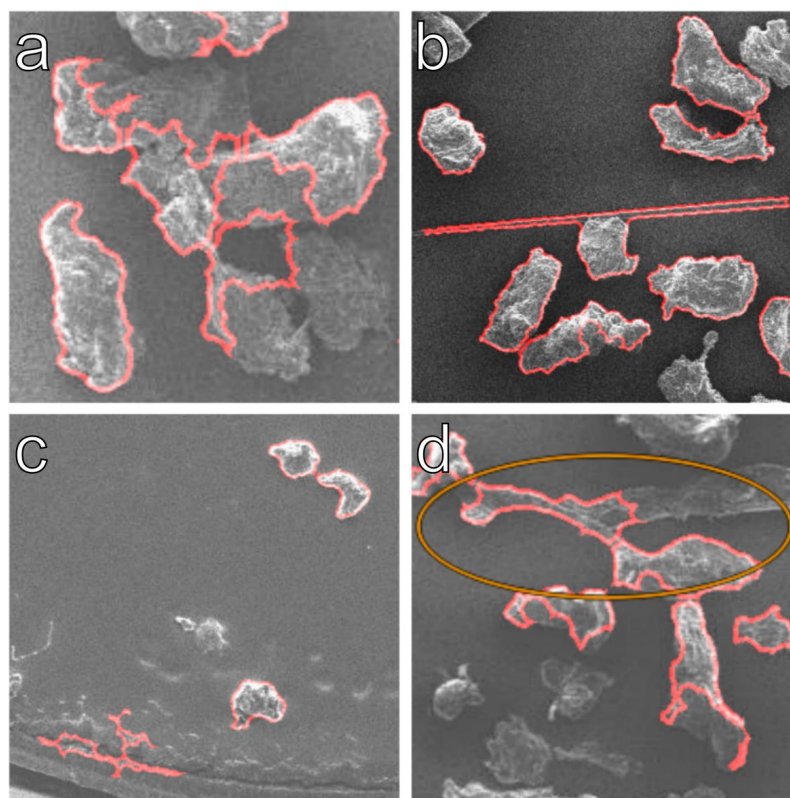
Figure 11. The SEM images show the limitations of the algorithm in terms of LDPE particle agglomerates (**a**), fiber overlap (**b**), phantom particles due to impurities (**c**), and over-segmentation of very elongated rough particles (**d**) for low contrast. The orange circle shows a location were the segmentation was applied successfully.

4. Conclusions

The developed and successfully tested algorithm performs a fully automatic particle size analysis and shape classification on a microscopic image series of pre-sieved, manufactured LDPE particles with a size of <300 µm and <800 µm. Pilot tests have shown that each magnification must be calibrated with an appropriate standard since a simple conversion of the scale bar leads to noticeable deviations. Although the best setting was tested on 11 images after being explored with two pilot images, it was only conditionally suitable for a further series of images. This was mainly due to the losses caused by the compressed image format and the low-contrast image quality. Image quality is an important prerequisite for achieving good results. Compressed image formats should not be used if possible. The algorithm was compared for size consistency with sieve fractions, and it is important to note that the sieve fraction itself is not error-free. A priori information about particle size obtained through particle sieving can be successfully used to improve the algorithm further. In addition, the collection of the MPPs has limitations on particle size due to filter pores or net sizes. Before conduction shape analysis, the particles underwent a pilot test to determine their geometry. It was deemed appropriate to assume that they were elliptical. The analysis of LDPE particles from the same sieve fraction prepared and microscopically examined by two different operators, one image series analyzed manually with ImageJ (I-series) and the other fully automatic with Octave (O-series), shows surprising similarities despite the many divergent parameters. Improved watershed segmentation enables the algorithm to separate smaller agglomerates with high probability at the correct location. By visually comparing input and output images, the accuracy of the results can be quickly checked, and the adjustment can be adapted to the respective image qualities. However, using a single setting and maintaining the same accuracy is impossible. A static, optimal setting for reliable evaluation of a series of images is possible but prone to error. Therefore, dynamic settings must be considered for future improvements.

References

1. Gigault, J.; ter Halle, A.; Baudrimont, M.; Pascal, P.-Y.; Gauffre, F.; Phi, T.-L.; El Hadri, H.; Grassl, B.; Reynaud, S. Current opinion: What is a nanoplastics? *Environ. Pollut.* **2018**, *235*, 1030–1034. [CrossRef] [PubMed]

2. Blair, R.M.; Waldron, S.; Phoenix, V.; Gauchotte-Lindsay, C. Micro- and Nanoplastic Pollution of Freshwater and Wastewater Treatment Systems. *Springer Sci. Rev.* **2017**, *5*, 19–30. [CrossRef]

3. Sharma, S.; Chatterjee, S. Microplastic pollution, a threat to marine ecosystem and human health: A short review. *Environ. Sci. Pollut. Res.* **2017**, *24*, 21530–21547. [CrossRef] [PubMed]

4. Haegerbaeumer, A.; Mueller, M.T.; Fueser, H.; Traunspurger, W. Impacts of micro- and nano-sized plastic particles on benthic invertebrates: A literature review and gap analysis. *Front. Environ. Sci.* **2019**, *7*, 17. [CrossRef]

5. Gebhardt, C.; Forster, S. Size-selective feeding of Arenicola marina promotes long-term burial of microplastic particles in marine sediments. *Environ. Pollut.* **2018**, *242*, 1777–1786. [CrossRef] [PubMed]

6. Wegner, A.; Besseling, E.; Foekema, E.M.; Kamermans, K.; Koelmans, A.A. Effects of nanopolystyrene on the feeding behavior of the blue mussel (*Mytilus edulis* L.). *Environ. Toxicol. Chem.* **2012**, *31*, 2490–2497. [CrossRef] [PubMed]

7. Vroom, R.J.E.; Koelmans, A.A.; Besseling, E.; Halsband, C. Aging of microplastics promotes their ingestion by marine. *Environ. Pollut.* **2017**, *231*, 987–996. [CrossRef]

8. Foster, K.A.; Yazdanian, M.; Audus, K.L. Microparticulate uptake mechanisms of in-vitro cell culture models of the respiratory epithelium. *J. Pharm. Pharmacol.* **2001**, *53*, 57–66. [CrossRef]

9. Kwon, W.; Kim, D.; Kim, H.-Y.; Jeong, S.W.; Lee, S.-G.; Kim, H.-C.; Lee, Y.-J.; Kwon, M.K.; Hwang, J.-S.; Han, J.E.; et al. Microglial phagocytosis of polystyrene microplastics results in immune alteration and apoptosis in vitro and in vivo. *Sci. Total Environ.* **2022**, *807*, 150817. [CrossRef]

10. Ragusa, A.; Svelato, A.; Santacroce, C.; Catalano, P.; Notarstefano, V.; Carnevali, O.; Papa, F.; Rongioletti, M.C.A.; Baiocco, F.; Draghi, S.; et al. Plasticenta: First evidence of microplastics in human placenta. *Environ. Int.* **2021**, *146*, 106274. [CrossRef]

11. Frère, L.; Paul-Pont, I.; Moreau, J.; Soudant, P.; Lambert, C.; Huvet, A.; Rinnert, E. A semi-automated Raman micro-spectroscopy method for morphological and chemical characterizations of microplastic litter. *Mar. Pollut. Bull.* **2016**, *113*, 461–468. [CrossRef]

12. Anger, P.M.; von der Esch, E.; Baumann, T.; Elsner, M.; Niessner, R.; Ivleva, N.P. Raman microspectroscopy as a tool for microplastic particle analysis. *TrAC Trends Anal. Chem.* **2018**, *109*, 214–226. [CrossRef]

13. Löder, M.G.J.; Kuczera, M.; Mintenig, S.; Lorenz, C.; Gerdts, G. Focal plane array detector-based micro-Fourier-transform infrared imaging for the analysis of microplastics in environmental samples. *Environ. Chem.* **2015**, *12*, 563–581. [CrossRef]

14. Löder, M.G.J.; Gerdts, G. Methodology Used for the Detection and Identification of Microplastics—A Critical Appraisal. In *Marine Anthropogenic Litter*; Bergmann, M., Gutow, L., Klages, M., Eds.; Springer: Berlin/Heidelberg, Germany, 2015; pp. 201–227. [CrossRef]

15. Primpke, S.; Wirth, M.; Lorenz, C.; Gerdts, G. Reference database design for the automated analysis of microplastic samples based on Fourier transform infrared (FTIR) spectroscopy. *Anal. Bioanal. Chem.* **2018**, *410*, 5131–5141. [CrossRef] [PubMed]

16. Mintenig, S.M.; Bäuerlein, P.S.; Koelmans, A.A.; Dekker, S.C.; Van Wezel, A.P. Closing the gap between small and smaller: Towards a framework to analyse nano- and microplastics in aqueous environmental samples. *Environ. Sci. Nano* **2018**, *5*, 1640–1649. [CrossRef]

17. Peez, N.; Janiska, M.C.; Imhof, W. The first application of quantitative 1H NMR spectroscopy as a simple and fast method of identification and quantification of microplastic particles (PE, PET, and PS). *Anal. Bioanal. Chem.* **2019**, *411*, 823–833. [CrossRef] [PubMed]

18. Peez, N.; Becker, J.; Ehlers, S.M.; Fritz, M.; Fischer, C.B.; Koop, J.H.E.; Winkelmann, C.; Imhof, W. Quantitative analysis of PET microplastics in environmental model samples using quantitative 1H-NMR spectroscopy: Validation of an optimized and consistent sample clean-up method. *Anal. Bioanal. Chem.* **2019**, *411*, 7409–7418, Erratum in *Anal. Bioanal. Chem.* **2019**, *411*, 7603. [CrossRef] [PubMed]

19. Rodríguez Chialanza, M.; Sierra, I.; Pérez Parada, A.; Fornaro, F. Identification and quantitation of semi-crystalline microplastics using image analysis and differential scanning calorimetry. *Environ. Sci. Pollut. Res.* **2018**, *25*, 16767–16775. [CrossRef] [PubMed]

20. Elert, A.M.; Becker, R.; Duemichen, E.; Eisentraut, P.; Falkenhagen, J.; Sturm, H.; Braun, U. Comparison of different methods for MP detection: What can we learn from them, and why asking the right question before measurements matters? *Environ. Pollut.* **2017**, *231*, 1256–1264. [CrossRef]

21. Stock, F.; Kochleus, C.; Bänsch-Baltruschat, B.; Brennholt, N.; Reifferscheid, G. Sampling techniques and preparation methods for microplastic analyses in the aquatic environment—A review. *TrAC Trends Anal. Chem.* **2019**, *113*, 84–92. [CrossRef]

22. Hidalgo-Ruz, V.; Gutow, L.; Thompson, R.C.; Thiel, M. Microplastics in the marine environment: A review of the methods used for identification and quantification. *Environ. Sci. Technol.* **2012**, *46*, 3060–3075. [CrossRef] [PubMed]

23. Koelmans, A.A.; Nor, N.H.M.; Hermsen, E.; Kooi, M.; Mintenig, S.M.; De France, J. Microplastics in freshwaters and drinking water: Critical review and assessment of data quality. *Water Res.* **2019**, *155*, 410–422. [CrossRef] [PubMed]

24. Uurasjärvi, E.; Hartikainen, S.; Setälä, O.; Lehtiniemi, M.; Koistinen, A. Microplastic concentrations, size distribution, and polymer types in the surface waters of a northern European lake. *Water Environ. Res.* **2020**, *92*, 149–156. [CrossRef] [PubMed]

25. Conkle, J.L.; Báez Del Valle, C.D.; Turner, J.W. Are We Underestimating Microplastic Contamination in Aquatic Environments? *Environ. Manag.* **2018**, *61*, 1–8. [CrossRef] [PubMed]

26. Hanvey, J.S.; Lewis, P.J.; Lavers, J.L.; Crosbie, N.D.; Pozo, K.; Clarke, B.O. A review of analytical techniques for quantifying microplastics in sediments. *Anal. Methods* **2017**, *9*, 1369–1383. [CrossRef]

27. Wills, B.A.; Finch, J.A. Particle Size Analysis. In *Wills' Mineral Processing Technology—An Introduction to the Practical Aspects of Ore Treatment and Mineral Recovery*, 8th ed.; Wills, B.A., Finch, J.A., Eds.; Butterworth-Heinemann: Boston, MA, USA, 2016; pp. 91–107. [CrossRef]

28. Buhr, E.; Senftleben, N.; Klein, T.; Bergmann, D.; Gnieser, D.; Frase, C.G.; Bosse, H. Characterization of nanoparticles by scanning electron microscopy in transmission mode. *Meas. Sci. Technol.* **2009**, *20*, 084025. [CrossRef]

29. Peregrina-Barreto, H.; Terol-Villalobos, I.R.; Rangel-Magdaleno, J.J.; Herrera-Navarro, A.M.; Morales-Hernández, L.A.; Manríquez-Guerrero, F. Automatic grain size determination in microstructures using image processing. *Measurement* **2013**, *46*, 249–258. [CrossRef]

30. Wang, Z.-M.; Wagner, J.; Ghosal, S.; Bedi, G.; Wall, S. SEM/EDS and optical microscopy analyses of microplastics in ocean trawl and fish guts. *Sci. Total Environ.* **2017**, *603–604*, 616–626. [CrossRef]

31. Shanthi, C.; Kingsley Porpatham, R.; Pappa, N. Image analysis for particle size distribution. *Int. J. Eng. Technol.* **2014**, *6*, 1340–1345.

32. Altuhafi, F.; O'Sullivan, C.; Cavarretta, I. Analysis of an Image-Based Method to Quantify the Size and Shape of Sand Particles. *J. Geotech. Geoenvironmental Eng.* **2013**, *139*, 1290–1307. [CrossRef]

33. Chen, S.; Li, Y.; Mawhorte, C.; Legoski, S. Quantification of microplastics by count, size and morphology in beverage containers using Nile Red and ImageJ. *J. Water Health* **2020**, *19*, 79–88. [CrossRef]

34. Girão, A.V. SEM/EDS and Optical Microscopy Analysis of Microplastics. In *Handbook of Microplastics in the Environment*; Rocha-Santos, T., Costa, M., Mouneyrac, C., Eds.; Springer International Publishing: Berlin/Heidelberg, Germany, 2020; pp. 1–22. [CrossRef]

35. Cabernard, L.; Roscher, L.; Lorenz, C.; Gerdts, G.; Primpke, S. Comparison of Raman and Fourier Transform Infrared Spectroscopy for the Quantification of Microplastics in the Aquatic Environment. *Environ. Sci. Technol.* **2018**, *52*, 13279–13288. [CrossRef] [PubMed]

36. Igathinathane, C.; Pordesimo, L.O.; Columbus, E.P.; Batchelor, W.D.; Methuku, S.R. Shape identification and particles size distribution from basic shape parameters using ImageJ. *Comput. Electron. Agric.* **2008**, *3*, 168–182. [CrossRef]

37. Moaveni, M.; Wang, S.; Hart, J.M.; Tutumluer, E.; Ahuja, N. Evaluation of Aggregate Size and Shape by Means of Segmentation Techniques and Aggregate Image Processing Algorithms. *Transp. Res. Rec.* **2013**, *2335*, 50–59. [CrossRef]

38. Olson, E.W. Particle Shape Factors and Their Use in Image Analysis—Part 1: Theory. *J. GXP Compliance* **2011**, *15*, 85–96.

39. Damadipour, M.; Nazarpour, M.; Alami, M.T. Evaluation of Particle Size Distribution Using an Efficient Approach Based on Image Processing Techniques. *Iran J. Sci. Technol. Trans. Civ. Eng.* **2019**, *43*, 429–441. [CrossRef]

40. Kooi, M.; Koelmans, A. Simplifying Microplastic via Continuous Probability Distributions for Size, Shape, and Density. *Environ. Sci. Technol. Lett.* **2019**, *6*, 551–557. [CrossRef]

41. Moura, D.S.; Pestana, C.J.; Moffat, C.F.; Hui, J.; Irvine, J.T.S.; Lawton, L. Characterisation of microplastics is key for reliable data interpretation. *Chemosphere* **2023**, *331*, 138691. [CrossRef]

42. Brandt, J.; Fischer, F.; Kanaki, E.; Enders, K.; Labrenz, M.; Fischer, D. Assessment of Subsampling Strategies in Microspectroscopy of Environmental Microplastic Samples. *Front. Environ. Sci.* **2021**, *8*, 579676. [CrossRef]

43. Valsesia, A.; Parot, J.; Ponti, J.; Mehn, D.; Marino, R.; Melillo, D.; Muramoto, S.; Verkouteren, M.; Hackley, V.A.; Colpo, P. Detection, counting and characterization of nanoplastics in marine bioindicators: A proof of principle study. *Micropl. Nanopl.* **2021**, *1*, 5. [CrossRef]

44. Le, T.-T.; Miclet, D.; Heritier, P.; Piron, E.; Chateauneuf, A.; Berducat, M. Morphology characterization of irregular particles using image analysis. Application to solid inorganic fertilizers. *Comput. Electron. Agric.* **2018**, *147*, 146–157. [CrossRef]

45. Hajihashemi, M.R.; Jiang, H. Gaussian random ellipsoid geometry-based morphometric recovery of irregular particles using light scattering spectroscopy. *J. Quant. Spectrosc. Radiat. Transf.* **2013**, *11*, 886–895. [CrossRef] [PubMed]

46. Sun, H.Q.; Luo, Y.J. Adaptive watershed segmentation of binary particle image. *J. Microsc.* **2009**, *233*, 326–330. [CrossRef] [PubMed]

47. Kwon, D.; Yeom, E. Shape evaluation of highly overlapped powder grains using U-Net-based deep learning segmentation network. *J. Vis.* **2021**, *24*, 931–942. [CrossRef]

48. Ivleva, N.P. Chemical Analysis of Microplastics and Nanoplastics: Challenges, Advanced Methods, and Perspectives. *Chem. Rev.* **2021**, *121*, 11886–11936. [CrossRef] [PubMed]

49. Zarfl, C. Promising techniques and open challenges for microplastic identification and quantification in environmental matrices. *Anal. Bioanal. Chem.* **2019**, *411*, 3743–3756. [CrossRef] [PubMed]

50. Schwaferts, C.; Schwaferts, P.; von der Esch, E.; Elsner, M.; Ivleva, N.P. Which particles to select, and if yes, how many? Subsampling methods for Raman microspectroscopic analysis of very small microplastic. *Anal. Bioanal. Chem.* **2021**, *413*, 3625–3641. [CrossRef]

51. Anger, P.M.; Prechtl, L.; Elsner, M.; Niessner, R.; Ivleva, N.P. Implementation of an open source algorithm for particle recognition and morphological characterisation for microplastic analysis by means of Raman microspectroscopy. *Anal. Methods* **2019**, *11*, 3483–3489. [CrossRef]

52. Dąbrowska, A.; Mielańczuk, M.; Syczewski, M. The Raman spectroscopy and SEM/EDS investigation of the primary sources of microplastics from cosmetics available in Poland. *Chemosphere* **2022**, *308*, 136407. [CrossRef]

53. Kefer, S.; Friedenauer, T.; Langowski, H.C. Characterisation of different manufactured plastic microparticles and their comparison to environmental microplastics. *Powder Technol.* **2022**, *412*, 117960. [CrossRef]

54. Von Der Esch, E.; Kohles, A.J.; Anger, P.M.; Hoppe, R.; Niessner, R.; Elsner, M.; Ivleva, N.P. TUM-ParticleTyper: A detection and quantification tool for automated analysis of (microplastic) particles and fibers. *PLoS ONE* **2020**, *15*, e0234766. [CrossRef] [PubMed]

55. Ehlers, S.M.; Manz, W.; Koop, J.H.E. Microplastics of different characteristics are incorporated into the larval cases of the freshwater caddisfly *Lepidostoma basale*. *Aquat. Biol.* **2019**, *28*, 67–77. [CrossRef]

56. Solomon, C.; Breckon, T. *Fundamentals of Digital Image Processing: A Practical Approach with Examples in Matlab*; Wiley-Blackwell: Chichester, UK, 2011. [CrossRef]

57. McAndrew, A. *A Computational Introduction to Digital Image Processing*, 2nd ed.; Chapman and Hall: London, UK; CRC: Boca Raton, FL, USA, 2015.

58. Jaglom, I.M.; Boltjanski, W.G. *Convex Figures*; Holt Rinehart and Winston: New York, NY, USA, 1961.

59. Preparata, F.P.; Shamos, M.I. *Computational Geometry: An Introduction*; Springer: New York, NY, USA, 1985.

60. Huang, Z.; Hu, B.; Wang, H. Analytical methods for microplastics in the environment: A review. *Environ. Chem. Lett.* **2023**, *21*, 383–401. [CrossRef] [PubMed]